Shelf–Open Ocean Exchange Forced by Wind Jets

MICHAEL A. SPALL AND JOSEPH PEDLOSKY

Woods Hole Oceanographic Institution, Woods Hole, Massachusetts

(Manuscript received 16 August 2017, in final form 27 November 2017)

ABSTRACT

The general problem of exchange from a shallow shelf across sharp topography to the deep ocean forced by narrow, cross-shelf wind jets is studied using quasigeostrophic theory and an idealized primitive equation numerical model. Interest is motivated by katabatic winds that emanate from narrow fjords in southeast Greenland, although similar topographically constrained wind jets are found throughout the world's oceans. Because there is no net vorticity input by the wind, the circulation is largely confined to the region near the forcing. Circulation over the shelf is limited by bottom friction for weakly stratified flows, but stratification allows for much stronger upper-layer flows that are regulated by weak coupling to the lower layer. Over the sloping topography, the topographic beta effect limits the deep flow, while, for sufficient stratification, the upper-layer flow can cross the topography to connect the shelf to the open ocean. This can be an effective transport mechanism even for short, strong wind events because damping of the upper-layer flow is weak. A variety of transients are generated for an abrupt onset of winds, including short topography Rossby waves, long topographic Rossby waves, and inertial waves. Using parameters representative of southeast Greenland, katabatic wind events will force an offshore transport of $O(0.4)$ Sv ($1\ \text{Sv} \equiv 10^6\ \text{m}^3\ \text{s}^{-1}$) that, when considered for 2 days, will result in an offshore flux of $O(5 \times 10^{10})\ \text{m}^3$.

1. Introduction

The high-latitude North Atlantic and Arctic Ocean represent an important source of freshwater for the global ocean (Carmack et al. 2016). Because the primary sources of this freshwater are from rivers in the Arctic Ocean and from runoff and ice melt on Greenland, it enters the North Atlantic over the shelf along the east coast of Greenland. It has long been recognized that this low-salinity water has the potential, should it get transported into the deep convection sites in the Greenland and Labrador Seas, to disrupt the large-scale thermohaline circulation (Stommel 1961). Such behavior has since been found in numerical models spanning a wide range of complexity (Manabe and Stouffer 1988; Rahmstorf et al. 2005; Hawkins et al. 2011). However, none of these basin-scale models had sufficient spatial resolution to correctly resolve the physics that govern the exchange of the low-salinity waters between the shelf and the open-ocean convection sites. These models circumvent this problem by directly introducing freshwater at the surface in the basin interior. In some regions, such as the Southern Ocean, the compensating transport of warm offshore waters onto the shelf, where it can melt ice, is also of great climatic importance. Thus, key unknowns in the link between the freshwater cycle and the stability of the meridional overturning circulation are the mechanisms that control the exchange of waters between the shelf and the open ocean.

The transition between the shelf and the open ocean is important and dynamically interesting because it is generally marked by a rapid change in bottom depth at the shelf break. Because flow tends to be along constant depth contours, the shelf break provides a strong barrier to exchange. There are many mechanisms that may lead to exchange across the shelf break, including wind forcing, eddy fluxes, filamenting and small-scale mixing, dense bottom plumes, and transport in the bottom boundary layer.

We focus here on one particular mechanism of exchange–episodic cross-shelf winds that are characterized by a relatively short along-shelf length scale and a long across-shelf length scale. Such asymmetric forcing is common adjacent to gaps in coastal mountain ranges, as is found near the glacial fjords in southeast Greenland. Downslope flow off the ice sheets results in intense along-fjord wind events called piteraqs. They have mean wind speeds of $20\ \text{m}\ \text{s}^{-1}$ and durations

Corresponding author: Michael Spall, mspall@whoi.edu

DOI: 10.1175/JPO-D-17-0161.1

of $O(1)$ day (Oltmanns et al. 2014). There are typically 4–8 such events per year, primarily in winter (Oltmanns et al. 2014; Jackson 2016; Spall et al. 2017). Similar orographically constrained atmospheric winds are found throughout the world's oceans, including in the southeast Pacific Ocean (McCreary 1989), the Red Sea (Zhai and Bower 2013), the Adriatic Sea (Belusic et al. 2013), and the South China Sea (Wang et al. 2008). The Gulf of Tehuantepec in the southeast Pacific Ocean is probably the most studied in terms of the ocean response to gap wind forcing. McCreary (1989) developed a 1.5-layer linear theory and nonlinear numerical model of the upper-ocean response to a localized wind jet. The primary response is the development of a dipole with a strong current directed downwind, flanked by weaker onshore flow on both sides. The basic pattern remains in the nonlinear regime, but mixing weakens the cyclonic side of the dipole and enhances the offshore propagation speed. The important limitation of this study, with regards to the southeast Greenland shelf, is the neglect of bottom topography.

While our motivation is exchange along the southeast coast of Greenland, the common nature of such wind jets justifies a wider understanding of the general problem of how isolated wind jets across the shelf to the open ocean can force exchange across the steep topography that characterizes the transition from shelf to open ocean. A linear, 2-layer quasigeostrophic theory and key nondimensional numbers are developed in section 2. A fully nonlinear primitive equation model is used to test the basic predictions from the theory in idealized, but representative, conditions in section 3, including a more extensive investigation of the time-dependent response to the wind. Final discussion and summary is given in section 4.

2. Theory

We consider in this section a linear, quasigeostrophic (QG) model of the circulation of a fluid driven over the shelf and slope topography shown in Fig. 1. The shelf, with a flat bottom, occupies the region $l \le y \le L$, while the slope region lies in $0 \le y \le l$. The y axis is directed onshore, and the x axis is parallel to the coast, forming a right-handed coordinate system with the y axis while z is measured upward.

a. Homogeneous fluid

We begin by considering a linear theory for the response of a homogenous fluid. Standard QG leads to a vorticity equation for the geostrophic streamfunction ψ obtained by first analyzing the Ekman layers on the free surface and bottom and incorporating the vertical

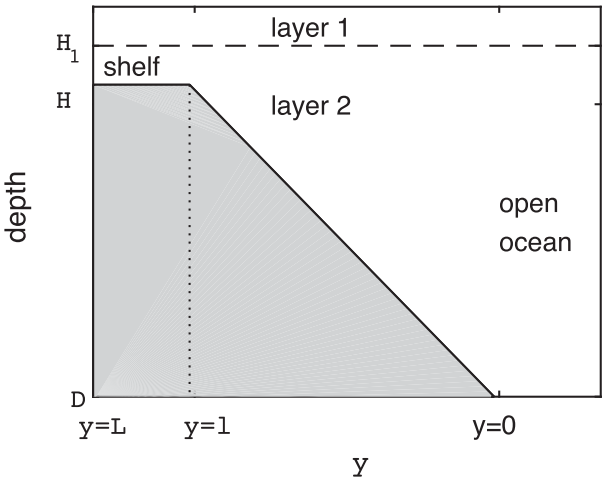

FIG. 1. The geometry of the shelf and slope.

velocity expelled from the Ekman layers into the vorticity balance, leading to the governing equation

$$\frac{\partial \nabla^2 \psi}{\partial t} + \epsilon \nabla^2 \psi + \beta_T \frac{\partial \psi}{\partial x} = \frac{\mathrm{curl}\tau}{\rho_0 H}, \tag{1}$$

where ϵ is the inverse spindown time, and β_T is the topographic beta term caused by the bottom slope and which is nonzero only in the interval $0 \le y \le l$. The inverse spindown time is given by $H/(\delta_E f)$, where δ_E is the Ekman layer thickness. In terms of the slope of the bottom $\partial h_b/\partial y$, the topographic beta parameter is $\beta_T = (f/H)\partial h_b/\partial y$ and is zero on the shelf and a constant on the slope. In QG theory the mean thickness H is treated as a constant. The interval in x is infinite in both positive and negative x. The wind stress curl that drives the circulation is chosen to represent the wind forcing of a localized outflow of air from a narrow fjord that exits onto the shelf and slope on the interval $-x_0 \le x \le x_0$. For simplicity, the curl is chosen to have the form

$$\mathrm{curl}\tau = \begin{cases} (\tau_0/x_0)\sin(\pi x/x_0), & |x| < x_0 \\ 0, & |x| \ge x_0 \end{cases}. \tag{2}$$

Note that the integral of the curl over the interval on which it acts is zero, that is, there is no net production of vorticity. On occasion we will employ a different representation of the forcing for analytical convenience but always a forcing that shares the property of no net vorticity input.

1) HOMOGENEOUS MODEL, STEADY SOLUTIONS

We start by considering the steady, unstratified solutions of (1). We recognize the limitations of these simplifications for the problem of interest but find it

useful to lay the foundation for the theoretical approach before moving on to consider stratification and time dependence.

Over the shelf the steady state is governed by

$$\epsilon\nabla^2\psi_{\rm sh} = \mathrm{curl}\tau/(\rho_0 H). \tag{3}$$

It is clear from (3) that this will yield a value of the streamfunction of order ϵ^{-1}. The subscript sh in this section will refer to the shelf solutions, while a subscript sl will refer to the solution over the slope.

On the other hand, for small $\epsilon \ll \beta_T x_0$, the steady solution on the slope will be seen to be much smaller than the steady solution on the shelf and will be of order $\epsilon/\beta_T x_0$ smaller. It follows that the solution on the shelf must vanish at $y = l$ to the order of that parameter. Thus,

$$\psi_{\rm sh} = -\frac{\tau_0}{\epsilon\rho_0 x_0 H}\frac{x_0^2}{\pi^2}\sin\pi\frac{x}{x_0} \times\left[1 - \frac{\sinh\pi(y-l)/x_0}{\sinh(L-l)/x_0} - \frac{\sinh\pi(y-L)/x_0}{\sinh\pi(l-L)/x_0}\right]. \tag{4}$$

In the slope region, with $\epsilon \ll \beta_T x_0$, the solution follows from a Sverdrup-like balance of the forcing with the topographic term. With the solution equal to zero to the right of the forcing region, that is, for $x > x_0$, we obtain

$$\psi_{\rm sl} = \frac{-\tau_0}{\beta_T\rho_0 x_0 H}\frac{x_0}{\pi}[1 + \cos(\pi x/x_0)]. \tag{5}$$

Note that the solution vanishes for $x \pm x_0$ as a consequence of the lack of a net vorticity input over the interval of the forcing.

The solution over the shelf represents a circulation consisting of two counterrotating cells, while the solution over the slope consists of a single cell. The two-cell regime over the shelf is limited to the shelf; that is, (4) shows that the flow, to that order, does not extend over the slope. The very weak slope flow in the y direction will produce a small, and so negligible, correction to the shelf flow, but imposing the condition that the derivative of the streamfunction with y is continuous at the shelf break, $y = l$, will produce a nonnegligible correction to the flow over the slope in a boundary layer of width $\delta_\beta = (\epsilon x_0/\beta_T)^{1/2}$. Introducing new, nondimensional boundary layer variables $\eta = (l - y)/\delta_\beta$ and $s = 1 - x/x_0$ leads to the diffusion equation for the correction $\phi_{\rm sl}(s, \eta)$ in the boundary layer region near $y = l$:

$$\frac{\partial^2\phi_{\rm sl}}{\partial\eta^2} = \frac{\partial\phi_{\rm sl}}{\partial s}. \tag{6}$$

Here, s is the timelike variable, and its positive direction is toward $-x$. The boundary condition for $\phi_{\rm sl}$ on $y = l$ is that its derivative in y matches the same as the derivative of $\psi_{\rm sh}$ at that point. The boundary condition that forces the solution, which is zero at $s = 0$, and vanishes for large η is

$$\frac{\partial\phi_{\rm sl}}{\partial\eta} = \delta_\beta\frac{\partial\psi_{\rm sh}}{\partial y} = -\delta_\beta U\sin\pi s \quad \eta = 0, \quad \text{and} \tag{7a}$$

$$U = \frac{\tau_o}{\epsilon\rho_0 x_0 H}\frac{x_0}{\pi}\left[-\frac{1}{\sinh\pi(L-l)/x_0} + \frac{\cosh\pi(L-l)/x_0}{\sinh\pi(L-l)/x_0}\right]. \tag{7b}$$

The analytic solution to (7a) can be found by the use of a Laplace transform in s. The form of the solution is rather opaque and is given as the convolution of two functions. It is more revealing to replace the sine function in (7a) with two Dirac delta functions of equal and opposite sign, so that (7a) is replaced by

$$\frac{\partial\phi_{\rm sl}}{\partial\eta} = -\delta_\beta(U/x_0)[\delta(s) - \delta(s-2)] \tag{8}$$

in the expectation that far from the forcing region the detailed structure of the forcing will be of minor importance and only its principal property, that is, of having no net integral in x, is of importance.

The use of the Laplace transform in the direction of increasing s leads to the more transparent solution

$$\phi_{\rm sl} = \delta_\beta\frac{U}{\pi^{1/2}}\left[\frac{e^{-\eta^2/4s}}{s^{1/2}}\mathcal{H}(s) - \frac{e^{-\eta^2/4(s-2)}}{(s-2)^{1/2}}\mathcal{H}(s-2)\right], \tag{9}$$

where $\mathcal{H}(x)$ is the Heaviside function, which is equal to 1 for positive values of its argument and is otherwise zero.

The solution is valid in the region $s > 0$, that is, in the region that includes the forcing and the region to the left of the forcing, where s is greater than 2. In that region the boundary layer consists of both terms in (9), which are of opposite sign and so the solution clearly goes to zero for large s. In fact, although each term in (9) diminishes like $s^{-1/2}$, the combination of the two terms can be shown to diminish at least as rapidly as $s^{-3/2}$. Therefore, the extent of the flow is limited to a region along the shelf break that is of the order of the forcing width. Figure 2a shows the rapid decay of the solution for $x < x_0$ that could be anticipated by a simple group velocity argument. For a disturbance that has a scale in y of the order of the thin boundary layer, the group velocity in the x direction would be of the order $\beta_T\delta_\beta^2$. Since the boundary layer width is $\delta_\beta = (\epsilon x_0/\beta_T)^{1/2}$, this yields a group speed toward positive s, that is, negative x of order ϵx_0, and so in a time of the order of the decay time ϵ^{-1}, the disturbance moves a distance of the order of the forcing width x_0. The fact that the two vorticity

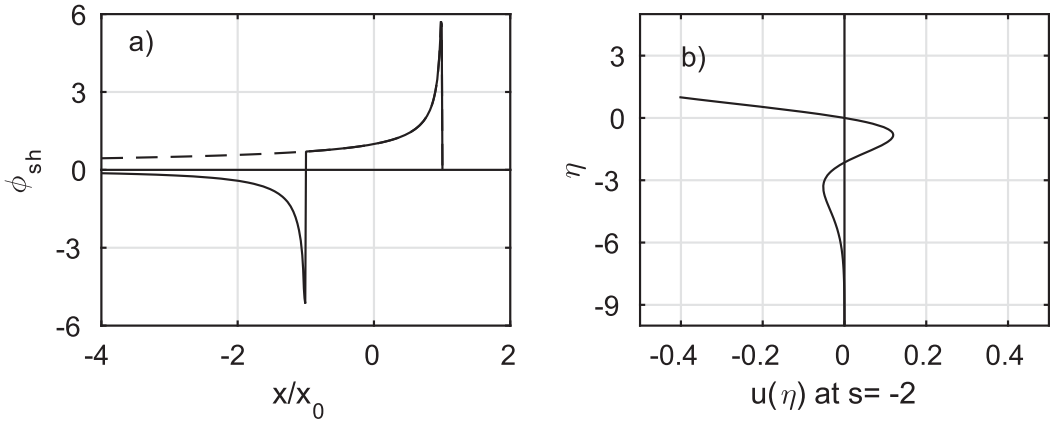

FIG. 2. (a) The value of the streamfunction in the boundary layer over the shelf at $(L - y)/\delta = 0.9$ in response to the forcing by two delta functions of opposite sign. The dashed curve shows the response for a single delta function at $x = x_0$, while the solid line shows the result of the interference of the two. (b) The form of zonal flow u as a function of η in the region to the left of the forcing. Note the recirculating flow.

sources are equal and opposite in sign leads to further interference and decay and in fact this is the major cause of the spatial limitation, as shown in Fig. 2a. Figure 2b shows the zonal velocity scaled by $\delta_\beta U/\pi^{1/2}$ as a function of the boundary layer coordinate. Note the rapid decay away from $y = l$ ($\eta = 0$), and note in particular the change in sign of the zonal velocity, indicating a recirculating boundary layer flow over the slope.

Thus, in the steady state there are three distinctly different regimes of flow produced by the forcing. The two-cell circulation on the shelf is the strongest, and there the transport streamfunction $\psi_{sh}H$ is order $(\tau_0 x_0)/(\epsilon\rho_0\pi^2)$. Taking typical parameters $\tau_0 = 1\,\mathrm{N\,m^{-2}}$, $\epsilon = 10^{-6}\,\mathrm{s^{-1}}$, and $x_0 = 10^5\,\mathrm{m}$ gives a transport of $O(10)$ Sv ($1\,\mathrm{Sv} \equiv 10^6\,\mathrm{m^3\,s^{-1}}$). At the shelf break the boundary layer flow is next in order of size, although it is a factor $(\epsilon/\beta_T x_0)^{1/2}$ smaller than the flow on the shelf. This boundary layer flow is not a direct continuation of the shelf flow over the slope. As its derivation shows, it is driven instead by the diffusion of the vorticity of the shelf flow onto a narrow region over the slope. The size of the streamfunction of the directly wind-driven flow over the slope is yet another factor $(\epsilon/\beta_T x_0)^{1/2}$ smaller than the boundary layer flow and a factor $(\epsilon/\beta_T x_0)$ smaller than the flow over the shelf. Taking typical parameters $f = 10^{-4}\,\mathrm{s^{-1}}$, $\epsilon = 10^{-6}\,\mathrm{s^{-1}}$, $\partial h_b/\partial y = 0.005$, $H = 250\,\mathrm{m}$, and $x_0 = 10^5$ gives $(\epsilon/\beta_T x_0) = 10^{-2}$, and so the diffusively driven flow over the slope is much weaker than the directly wind-driven flow over the shelf.

2) HOMOGENEOUS MODEL, TIME DEPENDENCE

Over the shelf, the solution (4) is the steady solution reached after the wind stress acts on the fluid. If we define that steady solution as $\overline{\psi}_{sh}$, the full solution, which represents the approach to that steady state, is

$$\psi_{sh} = \overline{\psi}_{sh}(1 - e^{-\epsilon t}). \tag{10}$$

The approach to steady state over the slope is dynamically more complex and reflects topographic Rossby wave dynamics. Since the steady solution is purely a function of x outside boundary layers on the slope, the full solution outside the boundary layer can be written as

$$\psi_{sl}(x,t) = \overline{\psi}_{sl} + \phi_{sl}(x,t). \tag{11}$$

Here, $\overline{\psi}_{sl}$ refers to the steady solution given by (5). The problem for the deviation can most easily be written for $v_{sl} = \partial\phi_{sl}/\partial x$:

$$\frac{\partial^2 v_{sl}}{\partial x \partial t} + \epsilon\frac{\partial v_{sl}}{\partial x} + \beta_T v_{sl} = 0, \qquad \text{and} \tag{12a}$$

$$v_{sl}(x,0) = -\mathrm{curl}\tau/\beta_T\rho_0 H, \tag{12b}$$

where (12b) is the initial condition.

The problems (12a) and (12b) can be most easily solved by using Laplace transforms and again simplifying the form of the forcing to

$$\mathrm{curl}\tau/\rho_0 H = \frac{\tau_0}{\rho_0 H}[\delta(x - x_0) - \delta(x + x_0)]. \tag{13}$$

It can be shown that the solution for $x > x_0$, that is, to the right of the forcing region is

$$v_{sl}(x,t) = \frac{\tau_0}{\rho_0 H}e^{-\epsilon t}(\beta_T(x + x_0)^{-1/2}t^{1/2}J_1\{2[\beta_T(x + x_0)t]^{1/2}\} - \beta_T(x - x_0)^{-1/2}t^{1/2}J_1\{2[\beta_T(x - x_0)]t^{1/2}\}), \tag{14}$$

where J_1 is the Bessel function of order one. Using (14) it can be shown that at any fixed time t, the solution decays

like $(x_0/x)^{3/2}$ for $x \gg x_0$. An example of this eastward propagation is given by the streamfunction as a function of x at time $t = 2/\beta_T x_0$ in Fig. 3. Of course this transient also decays in time at the scale-independent spindown rate after which the solution is the steady solution $\overline{\psi}_{sl}$. Nevertheless there is temporarily a limited propagation of short topographic Rossby waves in the positive x direction whose range is again limited by the absence of a net vorticity forcing.

b. *Stratified model*

The interaction of the wind-driven flow with the bottom topography and the bottom boundary layer has a powerful influence on the circulation. It is natural to wonder what changes would occur in the presence of a stable stratification. More precisely, what stratification would be required to isolate the flow from the bottom?

We will consider the standard quasigeostrophic two-layer model with the addition of a mixing term that couples the two layers by specifying a cross-isopycnal velocity across the interface between the two layers that is proportional to the displacement of the interface. If w_* is the cross-isopycnal velocity and h' is the upward displacement of the interface, we will model the diabatic mixing of the layer with the simple relationship

$$w_* = \gamma h', \tag{15}$$

where γ is a constant, which tends to damp interface anomalies. This can also be thought of as a crude parameterization of baroclinic instability, which also transfers momentum in the vertical and reduces the isopycnal slope.

The geostrophic streamfunction in each layer is related to the pressure perturbation in the usual manner, that is, $\psi_n = p_n/\rho_0 f$ and $n = 1, 2$, where the index n here refers to the upper and lower layer, respectively. At the same time the interface displacement can be written in terms of the pressure difference between the layers so that $h' = f(\psi_2 - \psi_1)/g'$, where g' is the reduced gravity between the two layers.

The linear, quasigeostrophic vorticity equation can then be written as

$$\frac{\partial}{\partial t}\left[\nabla^2\psi_1 - \frac{f^2}{g'H_1}(\psi_1 - \psi_2)\right] + \gamma\frac{f^2}{g'H_1}(\psi_2 - \psi_1) = \mathrm{curl}\tau/\rho_0 H_1 - \epsilon_i\nabla^2\psi_1, \quad \text{and} \tag{16a}$$

$$\frac{\partial}{\partial t}\left[\nabla^2\psi_2 - \frac{f^2}{g'H_2}(\psi_2 - \psi_1)\right] + \gamma\frac{f^2}{g'H_2}(\psi_1 - \psi_2) + \beta_T\frac{\partial\psi_2}{\partial x} = -\epsilon\nabla^2\psi_2. \tag{16b}$$

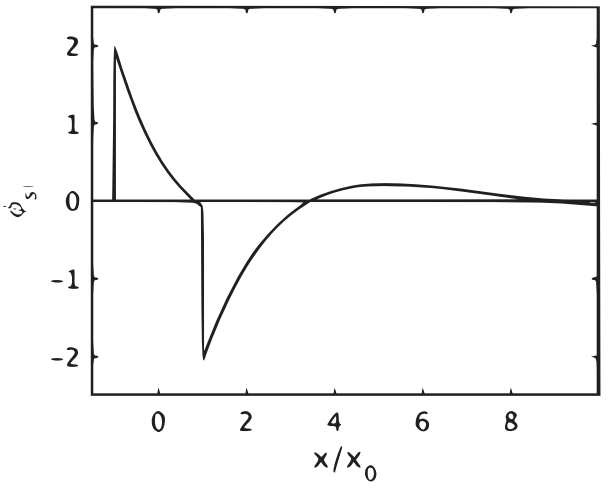

FIG. 3. The form of the radiation of short Rossby waves over the slope to the right of the forcing region for $t = 2/\beta_T x_0$. The abrupt jumps reflect the delta function forcing, but note the rapid decay of the wave amplitude caused by the interference of the two source terms of opposite signs.

The topographic β term is defined as before in terms of the bottom slope but with the mean layer thickness of the lower layer, namely, $\beta_T = (f/H_2)\partial h_b/\partial y$. The parameter ϵ is the inverse spindown time of the lower layer alone. The parameter ϵ_i is an admittedly artificial parameterization that provides an internal dissipation process for the upper layer. Throughout, we will assume $\epsilon_i \ll \epsilon, \gamma$.

1) STRATIFIED MODEL, STEADY SOLUTIONS

As in the case of the homogenous model, we first examine the solution over the flat shelf region. For steady motions, the equations reduce to

$$\gamma(\psi_2 - \psi_1)F_1 = \mathrm{curl}\tau/\rho_0 H_1 - \epsilon_i\nabla^2\psi_1, \tag{17a}$$

$$\gamma(\psi_1 - \psi_2)F_2 = -\epsilon\nabla^2\psi_2, \quad \text{and} \tag{17b}$$

$$F_n = f^2/g'H_n, \quad n = 1, 2. \tag{17c}$$

Multiplying (17a) and (17b) each by the layer thickness H_n leads to the barotropic balance, ignoring a small term proportional to ϵ_i:

$$\epsilon\nabla^2\psi_2 = \mathrm{curl}\tau/\rho_0 H_2. \tag{18}$$

Thus, in the steady state the vorticity imposed by the wind stress curl must be expunged by the bottom boundary layer. This gives an estimate of the steady response of the lower layer over the shelf. If the horizontal scale is x_0, that estimate is

$$\psi_2 = O\left(\frac{\mathrm{curl}\tau}{\epsilon\rho_0 H_2}x_0^2\right), \quad \text{and} \tag{19a}$$

$$\psi_1 = \psi_2 - \frac{\mathrm{curl}\tau}{\gamma F_1 \rho_0 H_1}, \tag{19b}$$

where (19b) makes use of (17a),

The ratio of the first term on the right-hand side of (19b) to the second term is given by the parameter P:

$$P = \frac{\gamma}{\epsilon}\frac{f^2 x_0^2}{g' H_2} = \frac{\gamma}{\epsilon}\frac{x_0^2}{R_{d2}^2}. \tag{20}$$

If this parameter is small the magnitude of the streamfunction in the upper layer will be far greater than that for the flow in the lower layer, even though the lower layer is essential in eventually balancing the vorticity input. It is clear from (20) that this will occur either when the stratification is great so that the deformation radius for the lower layer $R_{d2} = (g' H_2)^{1/2}/f$ is much greater than the scale of the forcing and/or when the dissipation of the motion in the bottom layer occurs more rapidly than vertical mixing by the cross-isopycnal flow, that is, when $\gamma \ll \epsilon$. If the inequality is reversed the response to the forcing will be essentially barotropic and governed by the dynamics outlined in the previous sections. Thus, either weak stratification or very strong cross-isopycnal flow will recover the barotropic dynamics of the previous sections. Otherwise the dominant flow is in the upper layer and is determined independently of the bottom boundary layer.

Over the slope region, the barotropic component of the flow is derived by multiplying each layer's equation by its basic constant thickness and adding, yielding (again assuming the smallness of ϵ_i)

$$\beta_T \frac{\partial \psi_2}{\partial x} = -\epsilon \nabla^2 \psi_2 + \mathrm{curl}\tau/\rho_0 H_2. \tag{21}$$

Thus, if $\beta_T x_0 \gg \epsilon$, the topographic equivalent of the Sverdrup regime, our estimate of the magnitude of the streamfunction in the lower layer would be

$$\psi_2 = O\left(\frac{\mathrm{curl}\tau}{\rho_0 \beta_T H_2}x_0\right), \tag{22}$$

while (17a) again yields (19b). It follows from that relation and (22) that the ratio of the streamfunction of the lower layer with respect to its counterpart in the upper layer is of the order of the parameter

$$P_{\beta T} = \frac{\gamma}{\beta_T x_0}\frac{x_0^2}{R_{d2}^2}, \tag{23}$$

so that, once again, if the stratification is large enough to make the deformation radius of the lower layer much larger than the horizontal scale of the forcing, the upper-layer motion will be much larger than that of the lower layer. This also occurs when the topographic Rossby constraint dominates the vertical mixing caused by the cross-isopycnal flux so that $P_{\beta T}$ is much less than one. This ratio may also be interpreted as the forcing length scale divided by the distance a topographic Rossby wave would propagate over the damping time scale.

Thus, in the strongly stratified case, with $\psi_1 \gg \psi_2$, both over the slope and over the shelf the dominant upper-layer flow outside any lateral boundary layers, is given by

$$\psi_1 = -\frac{\mathrm{curl}\tau/\rho_0 H_1}{\gamma F_1}, \tag{24}$$

with ψ_2 given by (22).

2) Stratified model, time dependence

We can discuss the response to an abrupt switch on of the forcing by the same approach as in our treatment of the barotropic problem. We write the total streamfunction as a sum of its steady solution, (22) and (24), and add a time-dependent term $\phi_n(x, y, t)$ that has as initial condition minus the steady solution. Our treatment in this section is limited to quasigeostrophic dynamics. In section 3, the numerical solution will also describe higher-frequency responses to abrupt forcing.

The functions ϕ_n satisfy (16a) and (16b). To obtain a qualitative idea of the nature of the approach to equilibrium, it is sufficient to look for solutions that are wavelike with a total wavenumber K, which we will suppose has the order of magnitude x_0^{-1}.

Over the shelf, the critical parameter is P, given by (20). When P is large the fluid behaves much like a homogeneous fluid and so the interesting case in dealing with the stratified case is when P is small. To simplify the algebra we will assume equal layer depths so that $F_1 = F_2 = F$. Searching for solutions of (16a) and (16b) of the form

$$\phi_n = A_n e^{\sigma t}\Phi_n(x, y), \quad \text{and} \tag{25a}$$

$$\nabla^2 \Phi_n = -K^2 \Phi_n, \tag{25b}$$

where σ is an eigenvalue and Φ is a structure function, we obtain for the perturbations on the shelf:

$$A_1 = -A_2(1 + \epsilon/\sigma), \quad \text{and} \tag{26a}$$

$$(\sigma + \epsilon)[\sigma(K^2 + F) + \gamma F] = F(\gamma + F). \tag{26b}$$

The first equation is obtained from the barotropic mode, while to obtain the dispersion relation we use (26a) and the equation for the upper layer (16a) to derive (26b).

For the case of small P, for which the steady solution in the upper layer is much greater than the streamfunction in the lower layer, there are two approximate

roots. The first root has $\sigma = -\epsilon$, and from (26a) this implies that the disturbance is limited to the lower layer where the dissipation is greatest. The lower layer thus adjusts more rapidly than the upper layer and reaches its relatively small steady flow state sooner than the more vigorously moving upper layer. This follows from the second root of the dispersion relation for which $\sigma = -\gamma F/K^2$ and $\psi_2 = 0$. These estimates depend on assuming that $Fx_0^2 \ll 1$, that is, that the stratification is strong enough to make the deformation radius much larger that the length scale of the forcing.

A similar dynamic holds over the slope. One mode, in the case of small P and $P_{\beta T}$, has a decay rate in which the mode is limited to the upper layer and so has a decay rate, as over the shelf, of $\sigma = -\gamma F/K^2$, while the second mode, limited to the lower layer, under the same parameter restriction, has $\sigma \approx -\epsilon + i\beta_T k/K^2$. Again these limits rely on a deformation radius much larger than the scale of the forcing, which we identify with $K^{-1} = O(x_0)$. Thus, for strong stratification the strongest motion is limited to the upper layer, while the lower layer spins down in this limit much more rapidly while propagating, briefly as a topographic Rossby wave.

3. Numerical model

The basic ideas developed with the quasigeostrophic theory in the previous section are now tested in an idealized configuration of the MITgcm primitive equation model (Marshall et al. 1997). In particular we seek to evaluate how effective strong, short pulses of wind stress directed across the shelf break are at transporting buoyant surface waters across the sloping topography and into the basin interior. The model uses Cartesian coordinates on a staggered C grid in the horizontal and fixed-depth coordinates in the vertical with a partial cell treatment of the bottom topography. The basic configuration shown in Fig. 1 is similar to that used for the theory in section 2. The domain extends 1080 km in the along-shelf direction and 576 km in the cross-shelf direction. The shelf is 226 km wide and 200 m deep, roughly modeled after the shelf along the east coast of Greenland (the results are not sensitive to the width of the shelf, provided that it is much wider than the internal deformation radius). There is a 50-km-wide region of uniform bottom slope down to 1000-m depth (bottom slope = 0.016). The offshore region is 300 km wide and has a flat bottom. The model domain has either closed boundaries on all sides ($\alpha = 0$) or periodic boundary conditions in the zonal direction ($\alpha > 0$), with no slip and no normal flow on the solid boundaries. The Coriolis parameter is $1.2 \times 10^{-4}\,\mathrm{s}^{-1}$ and constant. The horizontal grid spacing for most calculations is 3 km (those with narrow wind forcing of 10 km or less have a horizontal grid spacing of 500 m in the region of wind forcing). The model has 30 levels in the vertical, with 20 m thickness over the upper 460 m, gradually increasing to 130 m at the deepest level. Horizontal viscosity is parameterized with a Smagorinsky deformation–dependent Laplacian viscosity with nondimensional coefficient of 2.5 and a linear bottom drag with coefficient $4 \times 10^{-4}\,\mathrm{m\,s}^{-1}$. Vertical mixing is parameterized with the KPP scheme (Large et al. 1994) and background viscosity and diffusivity of $10^{-5}\,\mathrm{m}^2\,\mathrm{s}^{-1}$. Some calculations also include a term that restores salinity toward the initial resting profile with a time scale γ^{-1}. This is equivalent to the mass transport between layers in the QG model because it restores the density surfaces to their initial spatially uniform stratification.

The initial conditions are specified in terms of salinity, surface height, and an along-shelf flow in geostrophic balance with zero velocity at the bottom as

$$S(y,z) = S_0 + 0.5(S_m - S_0)\left\{1 - .5\alpha\left[1 + \tanh\frac{(y-l)}{L_f}\right]\right\} \times\left(1 + \tanh\frac{z - z_0}{\delta_z}\right), \quad \text{and} \tag{27a}$$

$$S_0 = (S_s + \alpha S_m)/(1+\alpha). \tag{27b}$$

This vertical profile approximates a 2-layer system with the transition at depth z_0 over thickness δ_z. The surface salinity over the shelf is S_s, the salinity at the bottom is S_m, and the surface salinity offshore of the shelf break is S_0. For $\alpha = 0$, the stratification is horizontally uniform (QG theory; surface salinity is S_s everywhere), while for $\alpha \gg 1$ the offshore stratification goes to zero while the stratification over the slope remains unchanged. An example of the initial conditions for $\alpha = 1.25$ is shown in Fig. 4, where the positive α results in an increase in the upper-layer salinity across the shelf break with a balancing westward geostrophic flow; $\alpha > 0$ is expected for the east Greenland region because the low-salinity waters originate on the shelf. The transition in stratification takes place over the slope in the upper layer, so that the density below z_0 is uniform across the slope and density at the surface transitions from S_s to S_0 over a horizontal scale L_f, centered at the shelf break $y = l$. This is balanced in the initial conditions by a westward, surface-intensified geostrophic flow above the shelf break: a shelfbreak jet. Density is related to salinity by a linear equation of state as $\rho = \rho_0 + \alpha_S(S - S_s)$ and $\alpha_S = 0.8\,\mathrm{kg\,m}^{-3}$.

The model is forced by a surface wind stress directed across the shelf toward the deep ocean. The wind is confined to a narrow jet, defined as

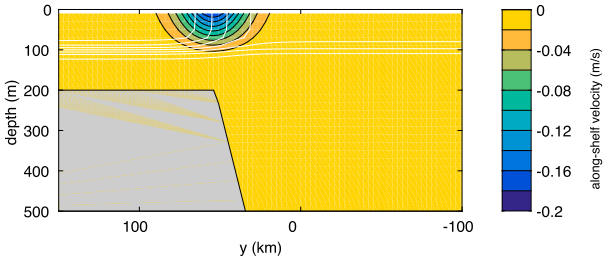

FIG. 4. Meridional section through the initial salinity (white contours; contour interval = 0.25) and along-shelf velocity (colors; $m\,s^{-1}$) in the vicinity of the shelf break. This initial condition has $\alpha = 1.25$, which gives a transition from high stratification over the shelf to weaker stratification offshore, with outcropping isohalines and a geostrophically balanced along-shelf jet. For $\alpha = 0$, the stratification over the shelf extends into the deep water, while for $\alpha = \infty$ all isohalines outcrop at the shelf break.

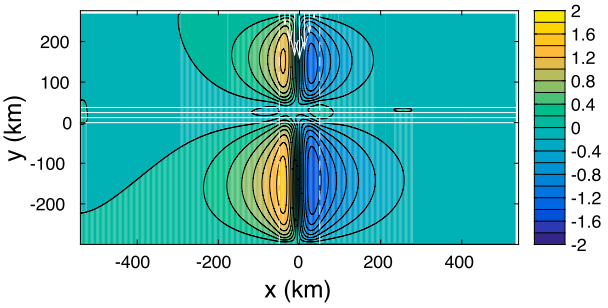

FIG. 5. Depth-integrated transport streamfunction (Sv) after 1 day of wind forcing. The solid white lines are the bottom topography (contours 300, 500, 700, and 900 m). The white dashed lines are the limits of the wind forcing; the pattern is indicated by the white vectors.

$$\tau^y = 0.5\tau_0[\cos(\pi x/x_0) + 1] \quad |x| \le x_0, \quad \text{and} \quad (28a)$$

$$\tau^y = 0 \quad |x| > x_0, \quad (28b)$$

where the maximum wind stress is τ_0, and x_0 is the horizontal decay scale of the wind. The stress yields a curl of the same form as our analytical model, so it shares the property of no net vorticity input. For calculations without the background restoring of density ($\gamma = 0$), the wind is held constant for 1 day and then turned off and the model is run for an additional 5 days. For those calculations with nonzero γ, the wind is held constant and the model is run until the transport across the sloping topography equilibrates. For the weakest restoring cases, this is 30 days. While this is not realistic with respect to the wind events along the east coast of Greenland, such long integrations allow us to more fully evaluate the underlying dynamics of the 2-layer system and its coupling to the bottom topography.

For the central case the wind stress $\tau_0 = 1\,N\,m^{-2}$, $S_s = 31$, $S_m = 33$, $\alpha = 0$, $z_0 = 100\,m$, $\delta_z = 20\,m$, and $x_0 = 50\,km$, which is typical of what is found over the east Greenland shelf in winter (Jackson 2016). This gives a baroclinic deformation radius over the shelf of $R_d = [g\alpha_S(S_m - S_s)z_0/\rho_0]^{1/2}/f = 10.3\,km$. Thus, this case falls in the range where the forcing length scale is large compared to the internal deformation radius. Cases with $\alpha > 0$ will be considered later in this section. The depth-integrated transport streamfunction at the end of the 1-day forcing period with $\gamma = 0$ is shown in Fig. 5. The flow is dominated by dipole pairs over both the shelf and flat interior, with only weak offshore transport connecting the two regions across the sloping topography (not evident at this contour level; see Fig. 7). The offshore-directed flow is confined to the region of offshore winds, with the onshore return flow extending over a larger horizontal scale to each side of the wind.

There is a suggestion of weak, closed recirculations over the slope, which are best revealed by the depth-integrated streamfunction as a function of x and time over the slope ($y = 15\,km$; Fig. 6). There are several different time-dependent features indicated in this figure. The first is the strong negative streamfunction that develops under the wind forcing during the first day. This is a result of the Ekman suction and pumping on either side of the jet. The initial response is symmetric in the x direction, but the high pressure signal rapidly propagates to the west along the topography. The low pressure also propagates westward and a short distance toward the east. After the wind is turned off we find short topographic Rossby waves radiating toward the east, as seen in our analytical model (eastward group speed, westward phase speed). Once the short waves have propagated east of the forcing region, a jet is left behind that transports water from the shelf toward the open ocean with return flows on both sides. This jet slowly drifts westward. There are also inertial waves that oscillate with a period of 0.6 days that stay trapped within the offshore jet.

The vertical structure of the flow across the slope over the final day of integration is shown in Fig. 7. The flow in the deep layer is close to zero while there is offshore flow centered under the wind jet with onshore flow flanking on both sides. The isopycnals are displaced vertically under the regions of maximum Ekman pumping and suction, such that the thermal wind shear balances the cross-slope flow. It is the combination of the bottom slope shutting down the deep flow together with this vertical displacement of the isopycnals that determines the cross-slope transport.

The offshore transport in the upper and lower layers, defined by salinity less than or greater than 32, is shown in Fig. 8. We define offshore transport as the integral of all flow with $v < 0$ at $y = 15\,km$. The net transport across

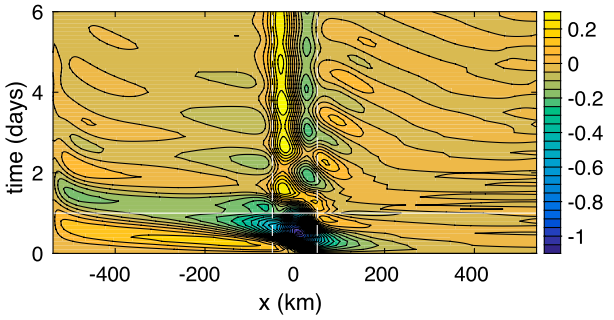

FIG. 6. Depth-integrated transport streamfunction (Sv) as a function of time and x at $y = 15$ km. The solid white line marks the end of wind forcing, and the dashed white lines indicate the limits of the wind forcing.

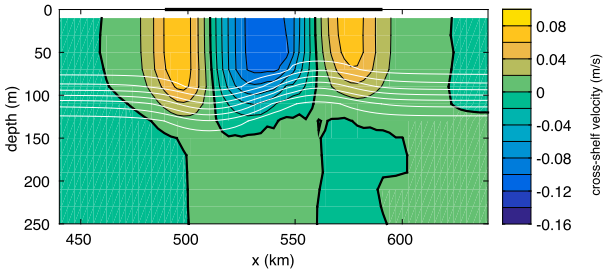

FIG. 7. Mean meridional velocity (colors; $\mathrm{m\,s^{-1}}$) and salinity (white contours; contour interval = 0.25) over the final day of integration down to a depth of 250 m at midslope ($y = 15$ km). The wind region of forcing is indicated by the thick black line. The bottom depth at this section is 800 m, so most of the flow is confined to the upper layer.

any section is very small. The inertial oscillation is very clear here. Most of the transport after the initial barotropic response propagates away is carried in the upper layer. The transport peaks near the end of the forcing period and remains nearly constant for the remainder of the calculation (when averaged over twice the period of the inertial waves). The offshore flow persists because the strong topographic slope effectively limits the transport in the lower layer, for example, (22); yet, the Ekman pumping/suction has deflected the interface such that thermal wind requires an offshore transport in the upper layer. With no interfacial friction and weak viscosity, the upper layer is slow to decay. Evidently, baroclinic instability is not effective at pumping momentum down into the lower layer on these time scales. Even though the wind forcing is very short in duration, the decoupling from the bottom provides an effective means of exporting the low-salinity shelf water across the slope. It is expected that this sense of circulation would continue until some other external event occurs to disrupt the flow, such as subsequent wind events or along-shelf advection by the background flow.

The two-layer quasigeostrophic potential vorticity equation can be used to get an estimate of the offshore transport that would be driven by an impulsive wind over a stratified ocean with a steep bottom slope. The vorticity equation for the upper layer, with $\gamma = 0$, is written as

$$\frac{\partial}{\partial t}\left[\nabla^2\psi_1 - \frac{f^2}{g'h_1}(\psi_1 - \psi_2)\right] = \frac{\mathrm{curl}\tau}{\rho_0 h_1}. \tag{29}$$

It will be assumed that the bottom slope is sufficiently steep so that, from (22), $\psi_2 \approx 0$. If we also assume that the crosswind length scale is much less than the alongwind length scale, then $\nabla^2\psi_1 \approx \psi_{1xx}$. Taking the form of wind stress given in (28a) and (28b), and assuming a form for the streamfunction as $\psi_1 = B(t)\cos(\pi x/L)$, the offshore transport in the upper layer $\mathcal{T} = \psi_1 h_1$ is found to increase linearly in time as

$$\frac{\partial \mathcal{T}}{\partial t} = \frac{\pi x_0 \tau_0}{\rho_0(\pi^2 + f^2 x_0^2/g'h_1)}. \tag{30}$$

For a wind forcing of $1\,\mathrm{N\,m^{-2}}$ applied for 1 day, this predicts an offshore transport of 0.4 Sv, close to what is found in the numerical model. The offshore transport averaged over the final day of the calculation is 0.36 Sv, similar to but slightly less than the peak predicted by (30). A more robust test of (30) is realized by carrying out a series of numerical calculations in which the stratification $g' = g\alpha_S(S_m - S_s)/\rho_0$ and the length scale of the forcing x_0 are varied. A comparison between model runs in which the stratification is varied and the

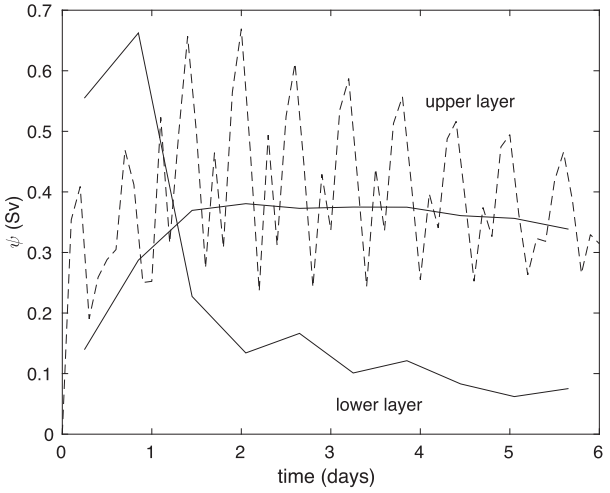

FIG. 8. Offshore transport (Sv) in the upper and lower layers at $y = 15$ km as a function of time. Solid lines are running averages over 1.2 days; the dashed line is the upper-layer transport every 0.1 days. Wind forcing is active for the first day and then turned off.

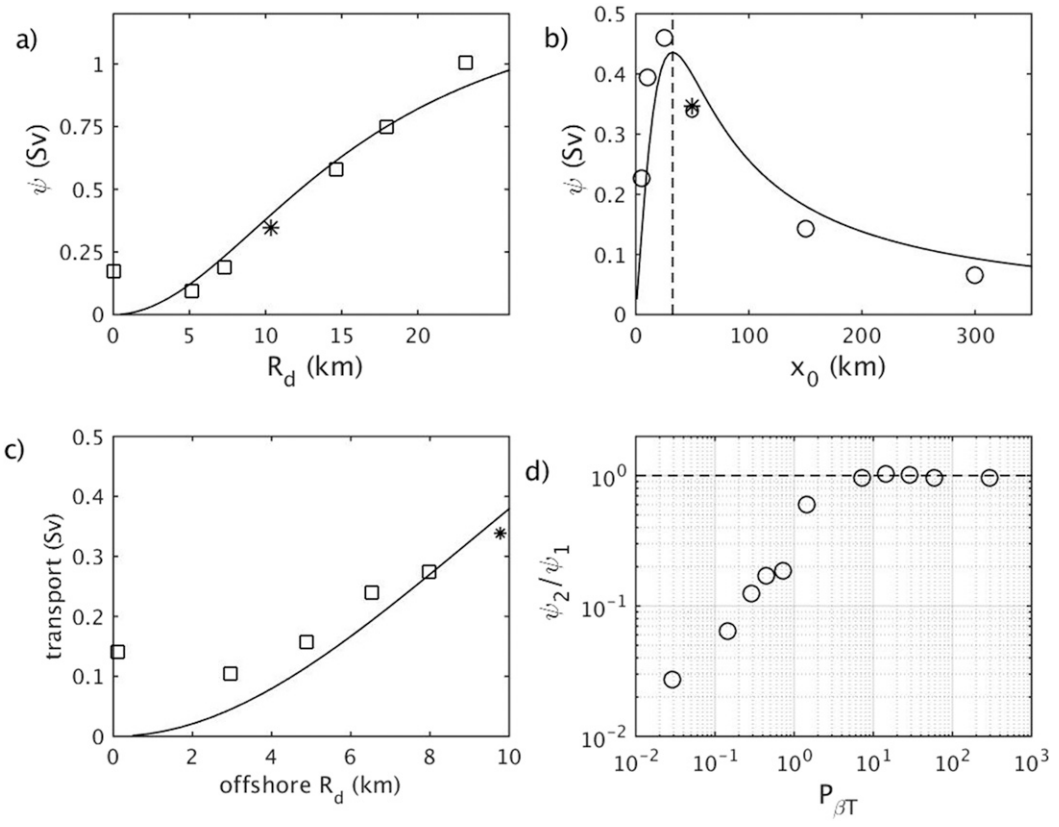

FIG. 9. Offshore transport in the upper layer for a series of numerical model calculations compared with (30) for variations in (a) initial stratification on the shelf, (b) length scale of the forcing, and (c) offshore deformation radius (through variations in α). The solid lines in (a), (b), and (c) are the transports predicted by (30), integrated for 1 day. (d) The ratio of the lower-layer streamfunction to the upper-layer streamfunction as a function of $P_{\beta T}$ for a series of model calculations varying γ and x_0.

prediction (30) is shown in Fig. 9a. The central case shown in Fig. 8 is indicated by the asterisk. There is generally close agreement for finite stratification. The offshore transport increases with increasing deformation radius, approximately linearly for stratifications representative of the east Greenland shelf. The transport found for zero stratification is a remnant of a barotropic topographic wave that is excited at time zero, also evident in the lower-layer transport in Fig. 8, which is not considered in the theory.

A second key parameter is the length scale of the forcing. A series of calculations were carried out with the central stratification (R_d = 10.3 km) and atmospheric forcing length scales x_0 varied between 5 and 300 km. The offshore transport in the model and from (30) is shown in Fig. 9b. There is close agreement with peak transports found close to $x_0 = \pi R_d$, as expected from (30). The circle nearly coincident with the asterisk (and those with smaller x_0) was carried out with the same forcing parameters but with a refined grid that had horizontal grid spacing of 500 m for $|x| < 100$ km, demonstrating convergence for the larger grid spacing. At smaller length scales relative vorticity becomes important and balances the vorticity input by the wind. At larger length scales the transport decreases because the vorticity input by the wind decreases.

The QG theory and above model calculations assumed that the stratification is horizontally uniform. However, given that the freshwater originates on the shelf and that the interior loses buoyancy to the atmosphere; in reality the surface in the basin interior is denser than that on the shelf. Up until this point, all of the numerical model calculations have been carried out with uniform initial stratification $\alpha = 0$ in order for consistent comparison with the QG theory. Now, the parameter α in (27a) and (27b) was varied between 0 and 100, resulting in an offshore change in salinity from surface to bottom that ranged between 0 and 2 and deformation radii that varied between 0 and 9.8 km. The offshore transport of low-salinity water was calculated as before at y = 15 km and is plotted against the offshore deformation radius in Fig. 9c. There is generally

increasing offshore transport with increasing offshore stratification. The solid line is the transport estimate given by (30) based on the offshore deformation radius. It generally compares well with the model results, although it does slightly underpredict the transport for large α. This is likely because there is some initial stratification over the slope, and the offshore transport further increases the stratification by advecting shelf water offshore. However, to leading order, the initial local stratification determines the offshore transport following (30). The finite transport at $R_d = 0$ is the same influence of barotropic Rossby waves, as seen in Fig. 9a.

The influence of coupling between the upper and lower layers is tested by varying the coupling parameter γ. The theory predicts that the nondimensional number $P_{\beta T}$ (23) controls the ratio of the transport in layer 2 to that in layer 1. The value of $P_{\beta T}$ was varied in the model by changing γ and/or the atmospheric forcing length scale x_0. The resulting range of $P_{\beta T}$ was between 0.03 and 300. The model was then run until the offshore transport equilibrated. For small $P_{\beta T}$, (weak coupling) the transport in layer 2 is much less than the transport in layer 1. This is because the weak momentum flow to the deep ocean is rapidly damped by bottom drag. The lower-layer transport increases roughly linearly with increasing $P_{\beta T}$ until this parameter is $O(1)$, at which point the flow is nearly barotropic and shows no further increases (Fig. 9d).

4. Discussion

The response of the coastal region to forcing representing the action of localized jets of wind issuing from oceanic fjords is strongly conditioned by the nature of the topography. Our theoretical model, although limited by the use of quasigeostrophic theory, identifies the main ingredients determining the response. Over the flat shelf region a strong circulation develops limited by bottom friction when the lateral scale of the forcing exceeds the deformation radius and permitting a barotropic response. On the other hand sufficiently strong stratification allows stronger motion, limited to the upper layer and constrained only by relatively weak mixing between the layers.

Over the slope region the topographic beta effect is dominating in the steady and low-frequency portion of the response. Strong enough stratification masks the effect of the topography but also limits the response of the wind driving largely to the upper layer except for high-frequency components of the response revealed in the numerical calculations of section 3. The result of sheltering the response from the topographic beta effect leads to a much larger transport over the slope in the steady state, even though limited to the upper layer. The localized nature of the forcing and response means that there is little net mass flux across the shelf. The dipole advects shelf water offshore and offshore water onto the shelf. The net property flux across the shelf break will depend on many other processes, such as time dependence, mixing, spatial variability, and ambient currents, so the theory provides an upper-bound estimate for the net property flux between the shelf and the open ocean.

The spatial extent of the time-dependent approach to equilibrium is seen in both the theory and numerical model results to be limited by the absence of a net vorticity source in the forcing. The interference of the positive and negative regions of the forcing leads to a rapid spatial decay of the waves produced by the onset of the forcing. At the same time, the presence of stratification induces a more rapid spinup of the lower layer to its equilibrium state.

Typical parameters for southeast Greenland are $\tau = 1\,\mathrm{N\,m^{-2}}$, $x_0 = 50\,\mathrm{km}$, $h_1 = 100\,\mathrm{m}$, and $g' = 0.015$. If the wind stress is applied for 1 day, from (30), the offshore transport will increase from 0 at time 0 to approximately 0.4 Sv. If it is assumed that this offshore transport persists for another day before being disrupted, this would give a total offshore flux of approximately $5 \times 10^{10}\,\mathrm{m^3}$. This is comparable to the observed flux forced out of Sermilik Fjord by katabatic winds (Jackson 2016; Spall et al. 2017). It is estimated that there are 4–8 strong wind events per year, so this would result in an offshore flux of $2\text{–}4 \times 10^{11}\,\mathrm{m^3}$ of low-salinity shelf water per year from winds associated with Sermilik Fjord. If we take a representative salinity of the shelf water as 31, this gives a total volume of freshwater fluxed offshore as approximately $20\text{–}40\,\mathrm{km^3\,yr^{-1}}$. This compares with a total southward freshwater flux of approximately $1500\,\mathrm{km^3\,yr^{-1}}$ in the East Greenland Current and $500\,\mathrm{km^3\,yr^{-1}}$ from glacial discharge on Greenland (Holfort et al. 2008). Additional offshore fluxes are expected downwind of other east Greenland fjords, such as Kangerdlugssuaq and Nansen Fjords. While the uncertainties are large, particularly the duration of the dipole circulation, these estimates of cross-shelf transports indicate that local wind-driven exchange represents an important component of the freshwater budget on the east Greenland shelf.

To provide simple, but clarifying, solutions to the question of wind-driven offshore flux across the slope, we have made several strong assumptions and neglected potentially important additional processes. Given that most of the strong katabatic wind events are found in winter, ice may be important in two ways. First, it acts as an intermediary in the transmission of momentum from the wind to the ocean. For very thick, immobile ice much

of the stress imparted from the wind on the ice is lost to internal ice stresses and is not transmitted to the ocean. On the other hand, for partial ice cover the amount of momentum transmitted to the ocean can be larger than for an ice-free ocean because of large air–ice and ice–ocean drag coefficients. The second way that ice may be important is as a direct means of freshwater flux. Ice will be advected both by direct wind stress and from the ocean advection beneath. So even in cases for which the bottom topography suppresses strong ocean currents, these winds may transport ice from the shelf to the basin interior. We have also for the most part neglected ambient currents, both in the interior and on the shelf. These currents may interact with the locally wind-driven flows studied here and alter their persistence or freshwater flux.

Acknowledgments. MAS was supported by the National Science Foundation under Grant OCE-1533170. We thank two anonymous reviewers for helpful comments and suggestions.

REFERENCES

Belusic, D., M. Hrastinski, Z. Vecenaj, and B. Grisogono, 2013: Wind regimes associated with a mountain gap at the northeastern Adriatic coast. *J. Appl. Meteor. Climatol.*, **52**, 2089–2105, https://doi.org/10.1175/JAMC-D-12-0306.1.

Carmack, E. C., and Coauthors, 2016: Freshwater and its role in the Arctic marine systems: Sources, disposition, storage, export, and physical and biogeochemical consequences in the Arctic and global oceans. *J. Geophys. Res. Biogeosci.*, **121**, 675–717, https://doi.org/10.1002/2015JG003140.

Hawkins, E., R. S. Smith, L. C. Allison, J. M. Gregory, T. J. Woollings, H. Pohlmann, and B. de Cuevas, 2011: Bistability of the Atlantic overturning circulation in a global climate model and links to ocean freshwater transport. *Geophys. Res. Lett.*, **38**, L10605, doi:10.1029/2011GL047208.

Holfort, J., E. Hansen, S. Osterhus, S. Dye, S. Jonsson, J. Meincke, J. Mortensen, and M. Meredith, 2008: Freshwater fluxes east of Greenland. *Arctic-Subarctic Ocean Fluxes*, R. R. Dickson, J. Meincke, and P. Rhines, Eds., Springer, 263–288.

Jackson, R. H., 2016: Dynamics of Greenland's glacial fjords. Ph.D. thesis, Massachusetts Institute of Technology and Woods Hole Oceanographic Institution, 158 pp.

Large, W. G., J. C. McWilliams, and S. C. Doney, 1994: Oceanic vertical mixing: A review and a model with a nonlocal boundary layer parameterization. *Rev. Geophys.*, **32**, 363–404, https://doi.org/10.1029/94RG01872.

Manabe, S., and R. J. Stouffer, 1988: Two stable equilibria of a coupled ocean–atmosphere model. *J. Climate*, **1**, 841–866, https://doi.org/10.1175/1520-0442(1988)001<0841:TSEOAC>2.0.CO;2.

Marshall, J., C. Hill, L. Perelman, and A. Adcroft, 1997: Hydrostatic, quasi-hydrostatic, and non-hydrostatic ocean modeling. *J. Geophys. Res.*, **102**, 5733–5752, https://doi.org/10.1029/96JC02776.

McCreary, J. P., 1989: The response of the coastal ocean to strong offshore winds: With application to the circulations in the Gulfs of Tehuantepec and Papagayo. *J. Mar. Res.*, **47**, 81–109, https://doi.org/10.1357/002224089785076343.

Oltmanns, M., F. Straneo, G. W. K. Moore, and S. H. Mernild, 2014: Strong downslope wind events in Ammassalik, southeast Greenland. *J. Climate*, **27**, 977–993, https://doi.org/10.1175/JCLI-D-13-00067.1.

Rahmstorf, S., and Coauthors, 2005: Thermohaline circulation hysteresis: A model intercomparison. *Geophys. Res. Lett.*, **32**, L23605, https://doi.org/10.1029/2005GL023655.

Spall, M. A., R. Jackson, and F. Straneo, 2017: Katabatic wind-driven exchange in fjords. *J. Geophys. Res. Oceans*, **122**, 8246–8262, https://doi.org/10.1002/2017JC013026.

Stommel, H., 1961: Thermohaline convection with two stable regimes of flow. *Tellus*, **13**, 224–230, https://doi.org/10.3402/tellusa.v13i2.9491.

Wang, G., D. Chen, and J. Su, 2008: Winter eddy genesis in the eastern South China Sea due to orographic wind jets. *J. Phys. Oceanogr.*, **38**, 726–732, https://doi.org/10.1175/2007JPO3868.1.

Zhai, P., and A. Bower, 2013: The response of the Red Sea to a strong wind jet near the Tokar Gap in summer. *J. Geophys. Res. Oceans*, **118**, 422–434, https://doi.org/10.1029/2012JC008444.